Published online 21 April 2020

Nucleic Acids Research, 2020, Vol. 48, No. 10 ***5603–5615***
doi: 10.1093/nar/gkaa238

Caveat mutator: alanine substitutions for conserved amino acids in RNA ligase elicit unexpected rearrangements of the active site for lysine adenylylation

Mihaela-Carmen Unciuleac[1], Yehuda Goldgur[2] and Stewart Shuman[1,*]

[1]Molecular Biology, Sloan-Kettering Institute, 1275 York Avenue, New York, NY 10065, USA and [2]Structural Biology Program, Sloan-Kettering Institute, 1275 York Avenue, New York, NY 10065, USA

Received February 20, 2020; Revised March 28, 2020; Editorial Decision March 30, 2020; Accepted April 01, 2020

ABSTRACT

Naegleria gruberi **RNA ligase (NgrRnl) exemplifies the Rnl5 family of adenosine triphosphate (ATP)-dependent polynucleotide ligases that seal 3′-OH RNA strands in the context of 3′-OH/5′-PO_4 nicked duplexes. Like all classic ligases, NgrRnl forms a covalent lysyl–AMP intermediate. A two-metal mechanism of lysine adenylylation was established via a crystal structure of the NgrRnl•ATP•$(Mn^{2+})_2$ Michaelis complex. Here we conducted an alanine scan of active site constituents that engage the ATP phosphates and the metal cofactors. We then determined crystal structures of ligase-defective NgrRnl-Ala mutants in complexes with ATP/Mn^{2+}. The unexpected findings were that mutations K170A, E227A, K326A and R149A (none of which impacted overall enzyme structure) triggered adverse secondary changes in the active site entailing dislocations of the ATP phosphates, altered contacts to ATP, and variations in the numbers and positions of the metal ions that perverted the active sites into off-pathway states incompatible with lysine adenylylation. Each alanine mutation elicited a distinctive off-pathway distortion of the ligase active site. Our results illuminate a surprising plasticity of the ligase active site in its interactions with ATP and metals. More broadly, they underscore a valuable caveat when interpreting mutational data in the course of enzyme structure-function studies.**

INTRODUCTION

Adenosine triphosphate (ATP)-dependent polynucleotide ligases are an ancient superfamily of nucleic acid repair enzymes that join 3′-OH and 5′-PO_4 DNA or RNA ends via a series of three metal-dependent nucleotidyl transfer steps (1). In step 1, the ligase reacts with ATP and a divalent cation to form a covalent ligase-(lysyl-Nζ)–AMP intermediate plus pyrophosphate. In step 2, AMP is transferred from ligase-adenylate to the 5′-PO_4 RNA or DNA end to form a DNA–adenylate or RNA–adenylate intermediate (AppRNA or AppDNA). In step 3, ligase catalyzes attack by an RNA or DNA 3′-OH on AppRNA or AppDNA to seal the two ends via a phosphodiester bond and release AMP. The step 1 auto-adenylylation reaction of ATP-dependent ligases is performed by a nucleotidyltransferase (NTase) domain that includes six peptide motifs (I, Ia, III, IIIa, IV and V) that form the nucleotide-binding pocket (1,2). Motif I contains the lysine that becomes covalently attached to the NMP.

In all DNA ligases, the NTase domain is fused at its C-terminus to an OB fold domain (1,3–8). By contrast, RNA ligases appear to have evolved many times, and independently, by NTase fusions to structurally diverse flanking domain modules. There are presently six structurally characterized ATP-dependent RNA ligase families exemplified by: bacteriophage T4 RNA ligase 1 (Rnl1 family) (9,10); T4 RNA ligase 2 (Rnl2 family) (11); *Pyrococcus abyssi* RNA ligase (Rnl3 family) (12); *Clostridium thermocellum* RNA ligase (Rnl4 family) (13,14), *Naegleria gruberi* RNA ligase (Rnl5 family) (15), and *Chaetomium thermophilum* tRNA ligase (Rnl6 family) (16,17). The Rnl1, Rnl2, Rnl3, Rnl4, and Rnl6-type enzymes consist of an N-terminal NTase domain linked to distinctive C-terminal domains. The C domain folds of these five RNA ligase clades are unrelated to one another and to the OB domains of DNA ligases.

By contrast, the Rnl5-type enzyme *N. gruberi* RNA ligase (NgrRnl) consists of an N-terminal OB fold module linked to a C-terminal NTase domain (15). NgrRnl is a template-directed ligase that seals 3′-OH/5′-PO_4 nicked duplexes in which the 3′-OH strand is RNA (18). NgrRnl prefers manganese as the metal cofactor for strand sealing. Rnl5-type ligases are found in: (i) diverse bacteria representing ten dif-

*To whom correspondence should be addressed. Tel: +1 212 639 7145; Email: s-shuman@ski.mskcc.org

ferent phyla; (ii) bacteriophages; (iii) archaea; and (v) unicellular eukarya, including amoebae and fungi (19). The activity of the Rnl5-type ligase from *Deinococcus radiodurans* helps protect this bacterium from killing by gamma radiation (20).

Key insights into the mechanism of lysine adenylylation by ATP-dependent ligases have emerged via crystallography of several exemplary DNA and RNA ligases in complexes with ATP (9,10,13,15,16,21). An instructive series of high-resolution crystal structures of NgrRnl captured snapshots of the enzyme at three discrete steps along the step 1 reaction pathway: ligase•Mn^{2+} apoenzyme; ligase•ATP•$(Mn^{2+})_2$ Michaelis complex; and covalent ligase-(lysyl-Nζ)–AMP•Mn^{2+} intermediate (15). These structures, and especially that of the Michaelis complex trapped by mutating the motif I Lys170 nucleophile to an isosteric methionine (Figure 1), highlighted a two-metal mechanism of nucleotidyl transfer, whereby: (i) an enzyme-bound penta-hydrated 'catalytic' metal coordination complex stabilizes the transition state of the ATP α phosphate; and (ii) a second metal coordination complex bridges the β and γ phosphates. The catalytic metal is engaged to the ligase by water-mediated contacts to three conserved carboxylate side chains: Asp172 in motif I; Glu227 in motif III; and Glu312 in motif IV (Figure 1). The Lys326 (motif V) and Arg149 side chains of the NTase domain engage the ATP phosphates, via a bifurcated interaction of Lys326 with α and γ phosphates and a bidentate interaction of Arg149 with the γ phosphate. There are no direct enzymic contacts to the ATP β phosphate. Amino acid side chains in the N-terminal OB domain engage the γ phosphate (via Arg4 and Lys121) and an associated metal complex (via water-mediated contact to Asp53) and thereby orient the pyrophosphate leaving group for in-line catalysis with stereochemical inversion at the AMP phosphate. This is evident in Figure 1, in which the lysyl-AMP adduct from the NgrRnl–AMP structure is superimposed on the ATP of the Michaelis complex. This overlay shows that the adenosine nucleosides superimpose almost perfectly, the Met170 side chain is indeed virtually isosteric to Lys170, and the Lys170-Nζ is situated 2.9 Å from the ATP α phosphorus in an apical orientation to the pyrophosphate leaving group (Nζ–Pα–O3α angle = 169°). The key role of the OB module of NgrRnl in lysine adenylylation was highlighted by characterization of a mutant enzyme, NgrRnl-ΔN, that lacks the N-terminal 126-aa segment. NgrRnl-ΔN was defective in overall 3′-OH/5′-PO_4 nick sealing and ligase adenylylation (step 1), but fully active in phosphodiester synthesis at a pre-adenylylated nick (step 3) (18).

The essentiality of certain conserved amino acids of the NTase motifs of DNA and RNA ligases was established even prior to the advent of crystal structures (and extended thereafter) by surveying the effects of alanine and conservative substitutions on overall ligation activity and the individual steps of the ligation pathway for several exemplary DNA and RNA ligases (4,22–32). However, there has been little in the way of structural analyses of the effects of ligase active site mutations, other than the affirmation that isosteric replacements of the motif I lysine nucleophiles with methionine in NgrRnl, T4 RNA ligase and *Escherichia coli* DNA ligase (an NAD^+-dependent enzyme) allowed faithful capture of a Michaelis complex of the respective enzyme adenylylation reactions (10). In the same vein, a motif I nucleophile Lys-to-Met mutation in *Mycobacterium tuberculosis* DNA ligase D eventuated in the crystal structure of a ligase•ATP•$(Mn^{2+})_2$ complex consistent with a two-metal mechanism for ATP-dependent DNA ligases (21).

Most rational mutagenesis strategies start with an alanine scan (33), which removes the side chain atoms beyond the β carbon and, in principle, imposes no steric or electrostatic interference. Alanine is presumed to be minimally disruptive of secondary structure when introduced in lieu of most amino acids (other than glycine or proline). The parsimonious interpretation of a loss-of-function upon alanine substitution for an active site constituent is that the missing enzymic functional group(s) are essential and that their simple absence causes the defect. Here we put this presumption to the test by conducting an alanine scan of the active site of NgrRnl and then determining the crystal structures of NgrRnl-Ala mutants, as purified and after incubation with ATP and manganese. We find that ligation-defective mutants K170A, R149A, E227A and K326A (as purified) crystallize as 'empty' apoenzymes with no significant alterations in tertiary structure and (with the exception of K326A) no significant changes in the active site other than the alanine change. The ligase-active mutant D172A crystallized as the covalent lysyl-AMP intermediate, albeit without an associated metal.

The surprising findings were that ligation-defective alanine mutations triggered drastic secondary changes in the active site of the ligase•ATP complex entailing dislocations of the ATP phosphates, altered enzymic contacts to ATP, and variations in the numbers and positions of the active site metals that collectively drove the active sites into off-pathway states incapable of catalyzing lysine adenylylation. Each alanine mutation elicited a distinctive off-pathway perversion of the ligase active site. In addition to informing our understanding of ligase mechanism and revealing unexpected plasticity of the ligase active site, our results raise important caveats regarding the interpretation of mutational data for enzymes.

MATERIALS AND METHODS

Recombinant NgrRnl

Native wild-type (WT) NgrRnl and NgrRnl mutants were produced in *E. coli* BL21(DE3) as His_{10}Smt3•NgrRnl fusions and isolated from a soluble bacterial extract by Ni-affinity chromatography. After cleaving the tag during overnight dialysis in the presence of the Smt3 protease Ulp1, tag-free NgrRnl was recovered in the flow-through fraction during a second Ni-affinity step. NgrRnl was purified further by DEAE-Sephacel anion-exchange chromatography and Superdex-200 gel filtration as described (15,18). Protein concentrations were determined by using the BioRad dye binding reagent, with bovine serum albumin as the standard.

Ligase substrate

The singly nicked duplex substrate was composed of an 18-mer RNA_{OH} strand and an 18-mer pDNA strand (labeled

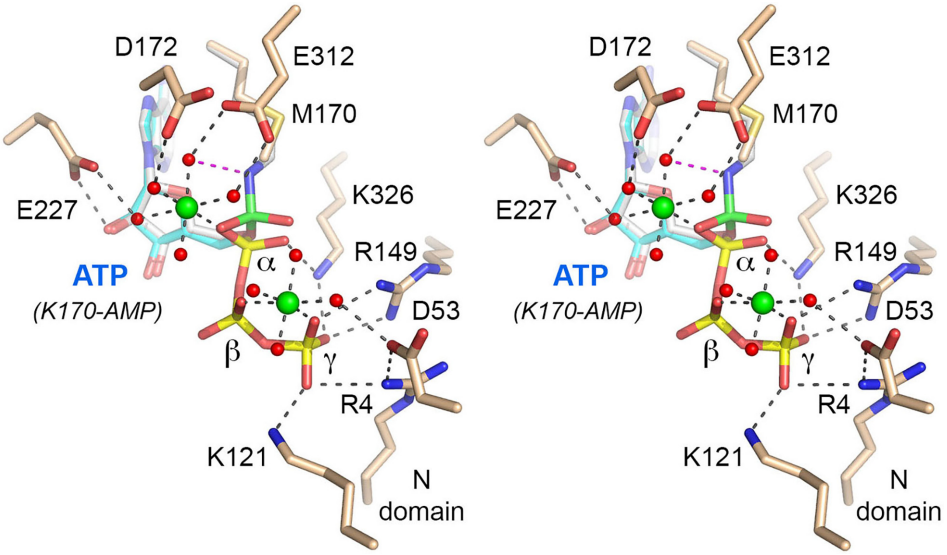

Figure 1. Stereo view of the active site of the NgrRnl^{K170M}•ATP•$(Mn^{2+})_2$ Michaelis complex. Amino acids and ATP are shown as stick models with beige and blue carbons, respectively; the ATP phosphorus atoms are colored yellow. Two Mn^{2+} ions and associated waters are depicted as green and red spheres, respectively. Atomic contacts are indicated by dashed lines. The superimposed lysyl–AMP adduct from the covalent intermediate structure (pdb 5COT) is shown with gray carbons and a green α phosphorus atom (to highlight the stereochemical inversion of the phosphorus center after lysine adenylylation).

with ^{32}P at the nick 5′-PO_4) annealed to a 36-mer DNA template strand. The 5′ ^{32}P-labeled oligonucleotides were prepared by label transfer from [γ ^{32}P]ATP catalyzed by T4 polynucleotide kinase, then purified free of ATP by electrophoresis through a non-denaturing 18% polyacrylamide gel. To form the nicked duplex, the radiolabeled pDNA strand, RNA_{OH} strand and DNA template strand were annealed at a 1:5:2 molar ratio in 200 mM NaCl, 10 mM Tris–HCl (pH 6.8), 1 mM ethylenediaminetetraacetic acid (EDTA) by incubation for 10 min at 65°C, 15 min at 37°C, and then 30 min at 22°C.

Nick sealing

Reaction mixtures (10 μl) constituted as described in the figure legends were incubated for 30 min at 37°C and then quenched by adding 10 μl of 90% formamide, 50 mM EDTA. The mixtures were analyzed by electrophoresis through a 15-cm 20% polyacrylamide gel containing 7.5 M urea in 44.5 mM Tris-borate (pH 8.3), 1 mM EDTA. The radiolabeled nucleic acids were visualized and the extent of sealing was quantified by scanning the gel with a Fuji BAS-2500 imagining apparatus.

5′-Adenylylated nicked duplex substrates

A pre-adenylylated 18-mer DNA strand (AppDNA) was prepared by RtcA-mediated AMP transfer to a 5′ ^{32}P-labeled pDNA strand (34). The AppDNA was separated from the pDNA by electrophoresis through a 20% polyacrylamide gel containing 7 M urea. After locating the strands by autoradiography, a gel slice containing the AppDNA species was excised and the AppDNA was eluted into 300 μl of 0.5 M ammonium acetate (pH 8.0), 10 mM magnesium acetate (pH 8.0), 1 mM EDTA, 0.1% sodium dodecyl sulphate (SDS) during overnight incubation at 4°C. The AppDNA strand was ethanol-precipitated and resuspended in 50 μl of 10 mM Tris-HCl (pH 8.0), 1mM EDTA. The pre-adenylylated nicked duplex substrate was formed by annealing the radiolabeled AppDNA strand, an 18-mer RNA_{OH} strand, and the complementary 36-mer DNA template strand at a 1:5:2 molar ratio in 200 mM NaCl, 10 mM Tris-HCl (pH 6.8), 1 mM EDTA.

Phosphodiester synthesis at a pre-adenylylated nick

Reaction mixtures (10 μl) containing 50 mM Tris-acetate (pH 6.0), 5 mM $MnCl_2$, 5 mM DTT, 1 pmol (0.1 μM) ^{32}P-labeled pre-adenylylated nicked duplex substrate and 1 pmol (0.1 μM) NgrRnl were incubated for 30 min at 37°C, then quenched with formamide, EDTA. The mixtures were analyzed by electrophoresis through a 15-cm 20% polyacrylamide gel containing 7.5 M urea in 44.5 mM Tris-borate (pH 8.3), 1 mM EDTA. The radiolabeled nucleic acids were visualized and the extent of AppDNA sealing was quantified by scanning the gel with a Fuji BAS-2500 imagining apparatus.

Crystallization

Crystals of recombinant NgrRnl mutants 'as purified' were grown by hanging drop vapor diffusion at room temperature after mixing on a cover slip 1 μl of protein solution (9.8 mg/ml K170A, 12 mg/ml D172A, 12 mg/ml E227A, 8.2 mg/ml R149A, or 10.2 mg/ml R4A-K121A) with 1 μl of reservoir solution containing 0.1 M HEPES, pH 6.5, 30% PEG6000. Crystals grew overnight. Single crystals were harvested, cryoprotected with parathone, and then flash frozen in liquid nitrogen. Mutant K326A (21.4 mg/ml) was mixed with an equal volume of precipitant solution containing 0.1 M HEPES, pH 6.5, 25% PEG6000. Crystals grew overnight. Harvested crystals were flask frozen directly

in liquid nitrogen. In a second series of crystallization experiments, the solutions of recombinant NgrRnl mutants were adjusted to 5 mM $MnCl_2$ plus 2 mM ATP and incubated for 15 min on ice before aliquots (1 μl) were mixed on a cover slip with 1 μl of reservoir solution containing 0.1 M HEPES, pH 6.5, 30% PEG6000 (K170A, E227A, K326A), 0.1 M HEPES, pH 6.5, 27% PEG6000 (R149A), or 0.1 M HEPES, pH 6.5, 25% PEG6000 (E312A). Crystals grew overnight. Single crystals of Mn/ATP-treated K170A, E312A, and E227A were harvested, cryoprotected with parathone, and then flash frozen in liquid nitrogen. Crystals of Mn/ATP-treated K326A and R149A were flask frozen directly in liquid nitrogen. A solution of WT NgrRnl (10 mg/ml) was adjusted to 1 mM PPi and incubated for 15 min on ice before an aliquot (1 μl) was mixed on a cover slip with 1 μl of reservoir solution containing 0.1 M HEPES, pH 6.5, 30% PEG6000. NgrRnl-K170M (10.5 mg/ml) was adjusted to 5 mM AMP plus 2 mM $MnCl_2$ and incubated for 15 min on ice before an aliquot (1 μl) was mixed on a cover slip with 1 μl of 0.1 M HEPES, pH 6.5, 30% PEG6000. Crystals grew overnight.

Diffraction data collection and structure determination

Diffraction data were collected continuously from single crystals at APS beamline 24ID-C. Indexing and merging of the diffraction data were performed in HKL2000 (35). The NgrRnl structures were solved by molecular replacement in Phenix (36), using PDB ID 5COT as the search model. The models were iteratively refined in Phenix and adjusted manually in O (37). Diffraction data and refinements statistics for the structures are compiled in Supplementary Table S1 for the six NgrRnl-Ala mutants crystallized 'as purified'; in Supplementary Table S2 for the structures of the five NgrRnl-Ala mutants pre-incubated with Mn/ATP; and in Supplementary Table S3 for WT NgrRnl treated with PP_i and NgrRnl-K170M pre-incubated with Mn/AMP.

RESULTS

Alanine scanning of NgrRnl active site constituents

The structure of the NgrRnl•ATP•$(Mn^{2+})_2$ step 1 Michaelis complex (Figure 1) guided an alanine scan of 8 active site amino acids that contact ATP and the two metal complexes: Arg4, Asp53, and Lys121 in the N-terminal OB domain; and Arg149, Asp172, Glu227, Glu312, and Lys326 in the NTase domain. The recombinant NgrRnl-Ala proteins were produced in *E. coli* and purified in parallel with WT NgrRnl. SDS-polyacrylamide gel electrophoresis (SDS-PAGE) verified the purity of the enzyme preparations with respect to the 38 kDa NgrRnl polypeptide (Figure 2A). Mutational effects on ligase activity were assessed by reaction of 0.1 μM NgrRnl with 0.1 μM nicked duplex nucleic acid substrate (composed of an 18-mer 5′ ^{32}P-labeled DNA strand and an unlabeled 18-mer 3′-OH RNA strand annealed to a 36-mer DNA strand; Figure 2B) in the presence of ATP and Mn^{2+}. Nick sealing resulted in the formation of a ^{32}P-labeled 36-mer RNApDNA strand that was resolved from the input ^{32}P-labeled 18-mer DNA by urea-PAGE. Under conditions in which the WT enzyme sealed virtually all of

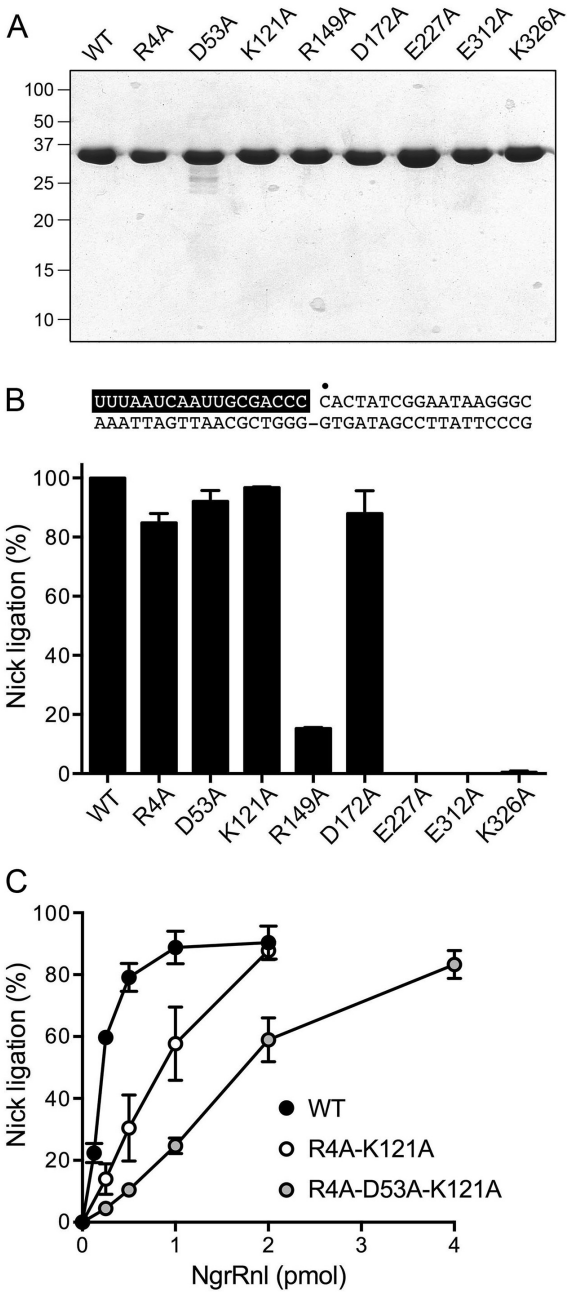

Figure 2. Alanine mutagenesis. (**A**) Recombinant NgrRnl proteins. Aliquots (6 μg) of WT NgrRnl and the indicated NgrRnl-Ala mutants were analyzed by SDS-PAGE. The Coomassie Blue-stained gel is shown. The positions and sizes (kDa) of marker polypeptides are indicated on the left. (**B**) Nick sealing. Reaction mixtures (10 μl) containing 50 mM Tris-acetate (pH 6.0), 5 mM $MnCl_2$, 0.2 mM ATP, 5 mM DTT, 1 pmol (0.1 μM) ^{32}P-labeled nicked duplex (shown at the *top,* with the ^{32}P label at the nick denoted by • and the RNA_{OH} strand depicted in white on a black background), and 1 pmol of WT NgrRnl or the indicated NgrRnl-Ala mutant were incubated for 30 min at 37°C. The reaction products were analyzed by urea-PAGE. The extents of nick ligation are plotted in bar graph format. Each datum is the average of two independent experiments; error bars denote the range of the two values. (**C**) Compound alanine mutants. Reaction mixtures (10 μl) containing 50 mM Tris-acetate (pH 6.0), 5 mM $MnCl_2$, 0.2 mM ATP, 5 mM DTT, 1 pmol (0.1 μM) ^{32}P-labeled nicked duplex substrate, and 0.25, 0.5, 1, 2 or 4 pmol of WT or mutant NgrRnl as specified were incubated for 30 min at 37°C. The extents of nick ligation are plotted as a function of input enzyme. Each datum is the average of three independent enzyme titration experiments ±SEM.

the input radiolabeled substrate, the E227A, E312A, and K326A mutants were inert (Figure 2B), signifying that the catalytic metal-binding Glu227 and Glu312 side chains and the ATP α and γ phosphate-binding Lys326 side chain are essential for strand joining. By contrast, alanine mutation of Asp172 that binds the catalytic metal and Asp53 that binds the non-catalytic metal did not grossly affect the extent of ligation (Figure 2B). Whereas mutation of the ATP γ phosphate-binding Arg149 side chain partially inactivated the enzyme (15% nick sealing), mutations of the two other ATP γ phosphate-binding residues, Arg4 and Lys121, were well tolerated (Figure 2B).

Based on the structure of the Michaelis complex (Figure 1), we considered the prospect that enzymic contacts of the N domain to the ATP γ phosphate and the non-catalytic metal might be functionally redundant. To test this idea, we produced a double-alanine mutant NgrRnl-R4A-K121A and triple-alanine mutant NgrRnl-R4A-D53A-K121A and assayed them for nick sealing activity as a function of input enzyme (Figure 2C). The specific activities of the NgrRnl-R4A-K121A and NgrRnl-R4A-D53A-K121A proteins, calculated from the slopes of the titration curves in the linear range of enzyme dependence (via linear regression in Prism), were 24 and 13%, respectively, of the WT specific activity. We surmise that γ phosphate contacts are indeed functionally redundant. We had shown previously that NgrRnl-ΔN, a mutant protein that lacks the N-terminal 126-aa OB domain, retains 4% of the nick sealing specific activity of full-length WT NgrRnl (18). By comparison to the 13% activity of the NgrRnl-R4A-D53A-K121A, we infer that a major function of the OB domain in nick sealing is to promote ligase adenylylation via its interactions with the PP_i leaving group.

Structural characterization of the ligase-defective NgrRnl-Ala mutants

Prior studies showed that recombinant WT NgrRnl produced in *E. coli* and purified through multiple chromatography steps is predominantly in the form of the covalent ligase–AMP complex (18), apparently by virtue of the enzyme's reaction with endogenous ATP (present at 9.6 mM in *E. coli* cytosol; 38) and metal cofactors. Indeed, crystals of recombinant WT NgrRnl grown in the absence of exogenous nucleotide or metals unambiguously had AMP covalently linked to the motif I Lys170 side chain in the active site, and a single divalent cation engaged to the AMP phosphate that we modeled as Mn^{2+} in light of the anomalous difference electron density overlying the metal atom (15). Here, in order to gain insights into the basis for the effects of alanine mutations on nick sealing activity, we grew crystals of five of the ligase-defective alanine mutants described above (E227A, E312A, K326A, R149A and R4A-K121A) and the ligase-inactive K170A mutant described previously (18). As a control, we also grew crystals of the ligase-active D172A mutant. We initially crystallized the recombinant proteins 'as purified'—that is, without any added nucleotide or metal cofactor—to see if the mutations affected formation of the ligase–AMP complex during protein production in bacteria. The crystallizations were successful and resulted in a suite of NgrRnl-Ala structures at 1.8 to 2.5 Å resolution in three different space groups and unit cells (Supplementary Table S1). [Note that we did not obtain adequately diffracting crystals of the defective E312A mutant as purified.] None of the ligase-defective NgrRnl-Ala mutants had a nucleotide or metal ion in the active site, suggesting a defect in ligase adenylylation. By contrast, the ligase-active D172A protein crystallized as the covalent ligase–AMP intermediate, albeit without an associated metal ion. The superimposed tertiary structures of the six mutants, color-coded and aligned with respect to their NTase domains, are shown in stereo view in Figure 3A. The alanine mutations elicited no gross structural changes. There was variability in the position of the OB domain by virtue of rigid body movements, by as much as 9.3 Å at the Asp61 Cα in the relatively 'closed' OB domain arrangement in K326A versus the 'open' configuration in D172A (Figure 3A). We presume these variations reflect differences in crystal packing.

Figure 3B provides a close-up stereo view of the active site amino acids (color-coded with respect to carbon atoms) in the six superimposed NgrRnl-Ala structures. The active site configuration in the D172A lysyl–AMP complex is virtually identical to that of the WT ligase–AMP intermediate (pdb 5COT) except for the absence of the catalytic metal ion. The instructive point is that the active site residues in the apoenzyme structures of the ligase-defective K170A, D227A, R149A, and R4A-K121A mutants were not perturbed *vis-à-vis* the active D172A enzyme. The active site constituents in the NTase domain were tightly superimposable in the set of mutants. The slight variations in the positions of Arg4 and Lys121 reflect the OB domain movements discussed above. By contrast, we see a significant perturbation of the active site in the K326A mutant apoenzyme, whereby the Arg149 side chain deviates from its normal position so that the cationic terminal guanidinium group occupies the position vacated by the loss of the cationic Lys326 terminal amino group (Figure 3B).

Structures of NgrRnl-Ala mutants after pre-incubation with ATP and manganese

Ligase-defective mutants K170A, E227A, E312A, K326A, and R149A were preincubated with 2 mM ATP and 5 mM manganese prior to mixture with precipitant solution. The crystallizations were successful and resulted in atomic structures at 1.55–2.5 Å resolution in three different space groups and unit cells (Supplementary Table S2). The superimposed tertiary structures of the five mutants, color-coded and aligned with respect to their NTase domains, are shown in stereo view in Figure 4A. Each of the NgrRnl-Ala mutants had a nucleotide and one or more manganese ions in the active site. A close-up stereo view of the nucleotides and metal ions in the five superimposed NgrRnl-Ala structures is shown in Figure 4B. The active sites of the K170A, E227A, K326A, and R149A proteins were populated by ATP, signifying that these mutants were grossly defective for lysine adenylation. The salient findings were that the trajectories of the ATP triphosphate moiety and associated metal ions differed dramatically between the various mutants (Figure 4B) and deviated significantly from that of the on-pathway Michaelis complex. As described in separate sections below, each of these alanine mutations per-

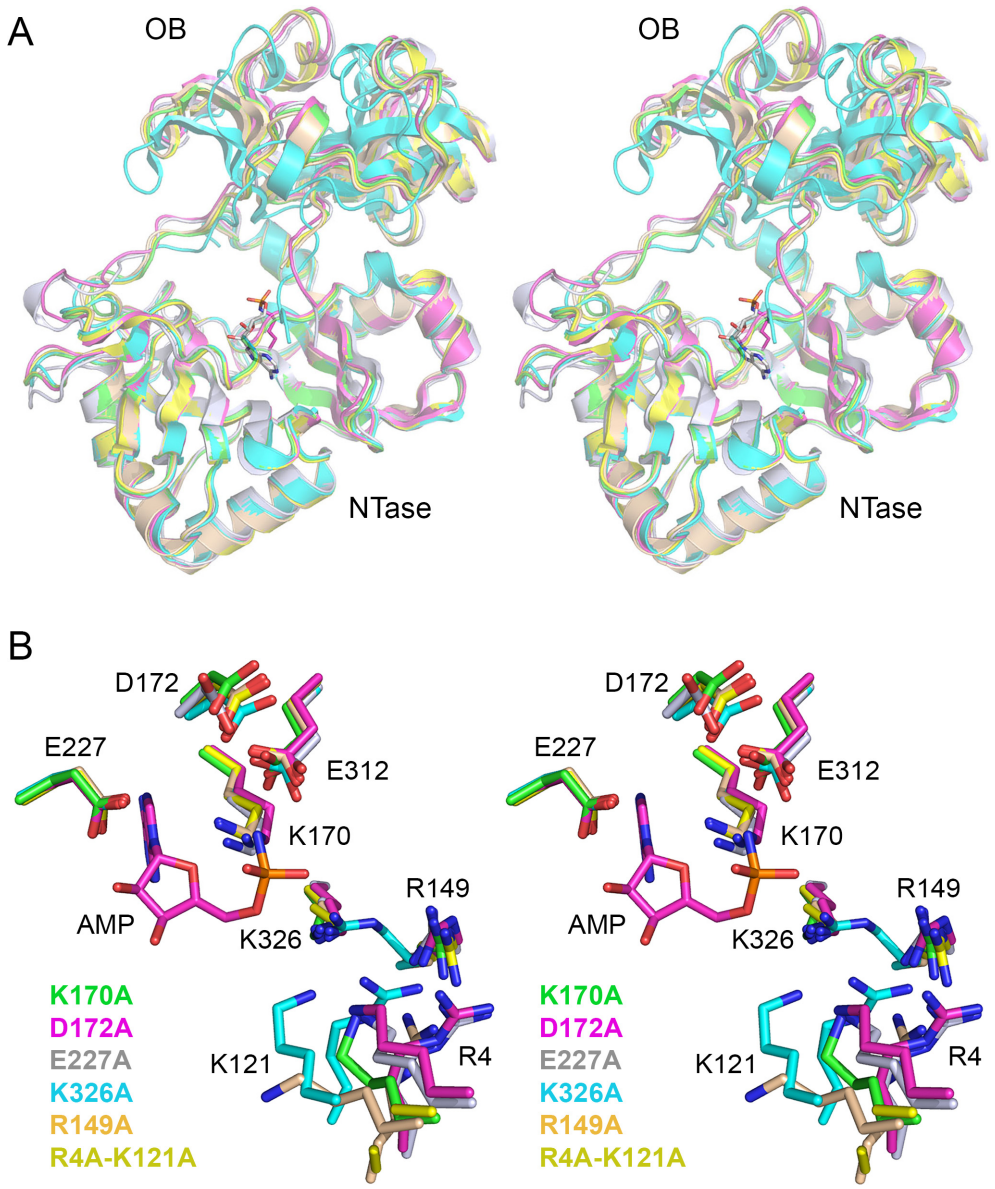

Figure 3. Structures of NgrRnl-Ala mutants crystallized as purified. (**A**) Stereo view of the superimposed tertiary structures of six NgrRnl alanine mutants, rendered as cartoon models and colored as specified in panel B. The structures were superimposed with respect to their NTase domains. The positions of the N-terminal OB domain relative to the NTase domain can vary slightly by virtue of rigid body movement. The active site is devoid of nucleotide in all cases except NgRnl-D172A, which crystallized as the covalent enzyme-AMP intermediate. (**B**) Close-up stereo view of the active site amino acids of the superimposed alanine mutants, with carbon atoms colored according to the scheme shown. Lys170 is Lys–AMP in the D172A mutant. The positions of the active site side chains are largely unaffected by the alanine mutations, with the exception of NgrRnl-K326A in which the Arg149 side chain is displaced from its normal position and now occupies the space vacated by loss of Lys326.

turbed enzymic interactions with the substrate and metals in unexpected ways that help explain their defects in lysine adenylylation.

By contrast, and to our surprise, preincubation of the E312A mutant with ATP and manganese yielded a structure at 2.0 Å resolution (in space group $P3_2$) of a covalent lysyl–AMP intermediate with a single catalytic pentahydrated manganese ion poised correctly in complex with the AMP phosphate (Supplementary Table S2). The water-mediated engagement of the manganese complex with the Asp172 and Glu227 side chains was the same in the E312A mutant NgrRnl–AMP intermediate as in the WT NgrRnl–AMP•Mn^{2+} structure, the only difference being the absence of the Glu312 side chain beyond the β carbon (not shown). There were no 'new' enzymic contacts by the E312A mutant to either of the two metal-bound waters normally coordinated to Glu312 in the WT NgrRnl–AMP•Mn^{2+} structure. That the NgrRnl E312A mutant crystallized as the covalent ligase–AMP intermediate was surprising because the equivalent motif IV Glu-to-Ala alanine change in other polynucleotide ligases, including the homologous Rnl5-family ligase from *D. radiodurans* (32), elicits a severe defect in lysine adenylylation when assayed in vitro (typically in a short time frame regime). We also solved a 2.6 Å structure of the

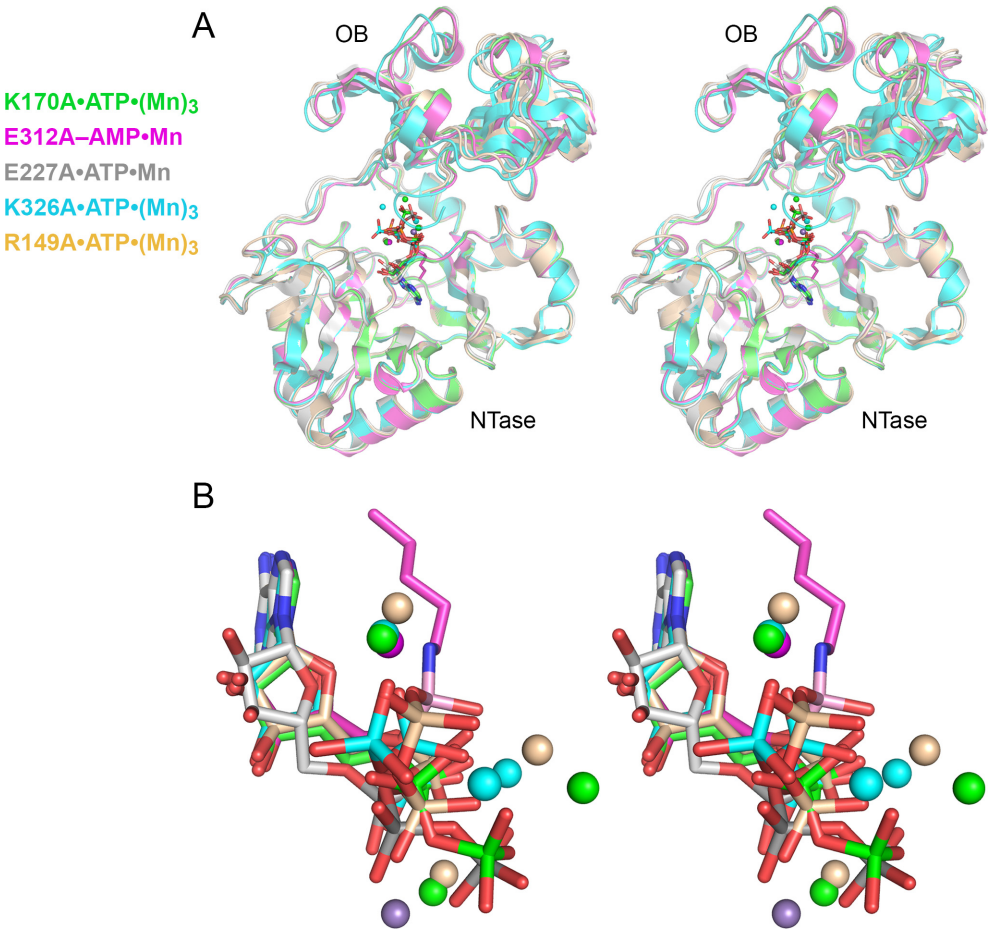

Figure 4. Structures of NgrRnl-Ala mutants crystallized after incubation with ATP and manganese. (**A**) Stereo view of the superimposed tertiary structures of five NgrRnl-Ala mutants, rendered as cartoon models with active site nucleotides depicted as stick models and variable numbers of manganese ions shown as spheres. The models are colored as specified on the *left*. The structures were superimposed with respect to their NTase domains. (**B**) Close-up stereo view of the active sites of the superimposed alanine mutants, with amino acid and nucleotide carbon atoms and manganese ions colored according to the scheme shown in panel A. The active site contains ATP in all cases except NgrRnl-E312A, which crystallized as the covalent enzyme-AMP intermediate in complex with a single manganese ion.

E312A mutant mixed with ATP and manganese in a different space group ($P4_12_12$) and found that it, too, contained a covalent Lys170–AMP adduct and an adjacent manganese ion (not shown). We suspect that the prolonged exposure of the E312A mutant to ATP and manganese during the crystallization experiments allowed the step 1 reaction to occur.

Off-pathway K170A•ATP•$(Mn^{2+})_3$ active site structure

Figure 5A shows a detailed stereo view of the active site of the K170A•ATP complex at 1.95 Å resolution. Comparison to the K170M•ATP Michaelis complex reveals unexpected and profound perturbations of enzymic contacts to ATP and metal ions as a consequence of the loss of the γ, δ, and ε atoms of amino acid 170. Absent the motif Lys170 side chain, the motif V Lys326 side chain is displaced from its normal position to occupy that of the Lys170-Nζ nucleophile, such that Lys326-Nζ replaces Lys170-Nζ in its salt bridge to Glu312 (Figure 5A). The position of the ATP α phosphorus shifts by 1.8 Å. The Lys326-Nζ is 3.9 Å from the α phosphorus in an orthogonal orientation to the pyrophosphate leaving group (Lys326-Nζ–Pα–O3α angle = 101°). This arrangement precludes Lys326 acting as a nucleophile for ligase adenylylation in lieu of Lys170. As a consequence of the movement of the ATP α phosphate, a water replaces an ATP α phosphate oxygen as the sixth ligand in the octahedral catalytic manganese coordination complex and the catalytic manganese is 5.7 Å away from the nearest ATP α phosphate oxygen. Thus, there is no potential for metal ion stabilization of a transition state for lysine adenylylation in the active site structure of K170A•ATP. The water-mediated contacts of Asp172, Glu227, and Glu312 to the catalytic manganese in the K170A structure echo those of the Michaelis complex and the ligase–AMP intermediate. The new sixth water in the K170A catalytic metal complex makes hydrogen bonds to the ATP β phosphate oxygens (Figure 5A). A second manganese ion in the K170A•ATP structure is the analog of the non-catalytic metal in the Michaelis complex, albeit shifted by 1.8 Å and contacting only the ATP γ phosphate rather than bridging the β and γ phosphates as in the Michaelis complex (Figure 5A). The other five sites in this metal complex are filled by an

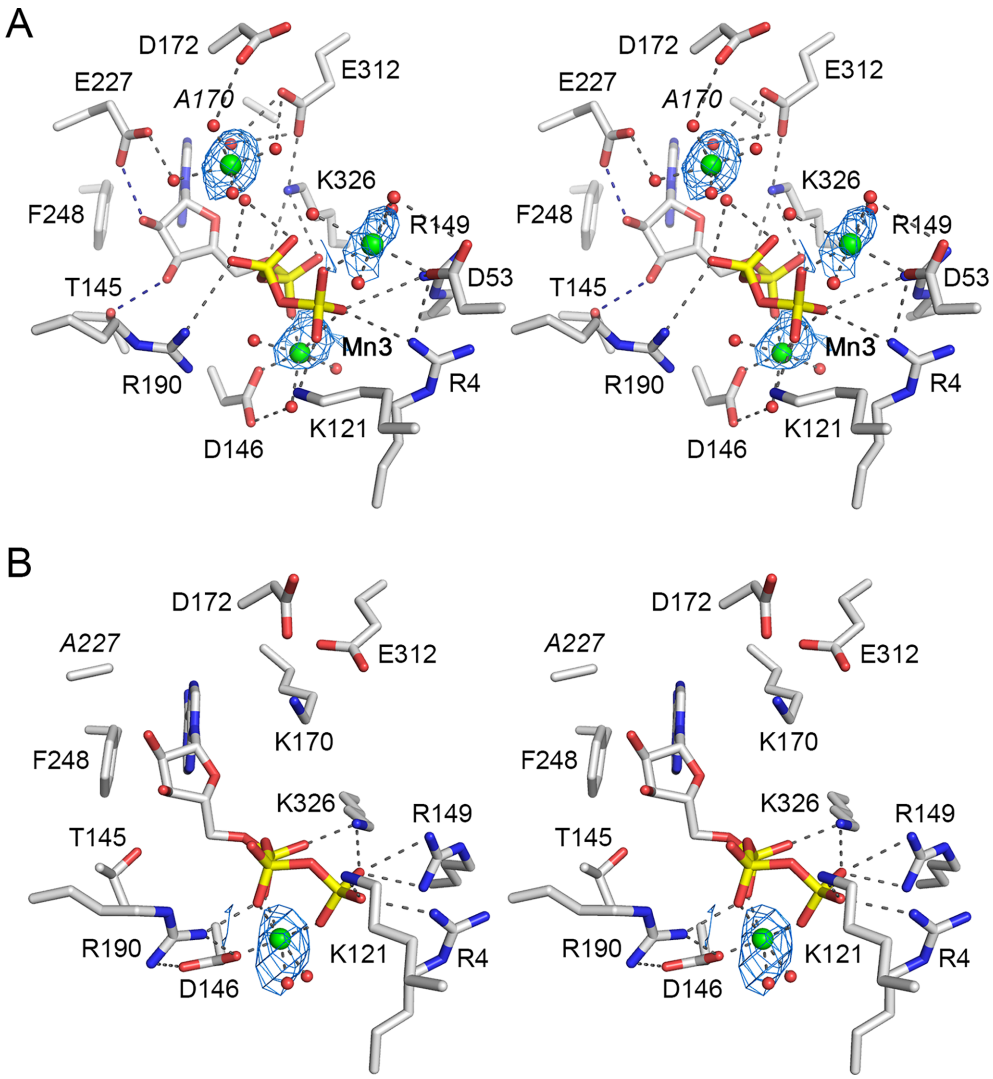

Figure 5. Off-pathway K170A•ATP•$(Mn^{2+})_3$ and E227A•ATP•Mn^{2+} active site structures. Stereo views of the K170A•ATP•$(Mn^{2+})_3$ (panel **A**) and E227A•ATP•Mn^{2+} (panel **B**) active sites. Amino acids and ATP are rendered as stick models. The Ala mutant side chains *A170* (panel A) and *A227* (panel B) are labeled in italics. Manganese ions are depicted as green spheres; waters as red spheres. Atomic contacts are denoted by dashed lines. Anomalous difference maps around the manganese atoms are depicted in blue mesh, contoured at 2 σ.

Asp53-Oδ2 and four waters, one of which is in turn coordinated by Asp53-Oδ1 (Figure 5A). Enzymic contacts to the γ phosphate from Arg4, Lys121 and Arg149 are analogous to those in the Michaelis complex. A remarkable feature of the K170A•ATP active site is the acquisition of a third manganese ion (labeled Mn3 in Figure 5A) that bridges the β and γ phosphates. The other four sites in this octahedral metal complex are occupied by Asp146-Oδ1 and three waters, one of which is coordinated by Asp146-Oδ2 (Figure 5A). [Note that Asp146 makes no atomic contacts in the Michaelis complex.] Arg149, which does not contact ATP in the Michaelis complex, reorients in the K170A mutant so as to interact with the ATP β phosphate.

Off-pathway E227A•ATP•Mn^{2+} active site structure

Figure 5B shows a stereo view of the E227A•ATP complex at 2.5 Å resolution. The salient finding is that loss of the metal-binding Glu227 side chain results in failure to assimilate the catalytic manganese into the ligase active site. This leads to significant warping of the conformation and contacts of the ATP. Whereas the adenine base stacks normally on Phe248, the loss of the hydrogen bond between Glu227 and the ribose 2′-OH results in rotation of the sugar about the glycosidic bond and severance of the hydrogen bond between Thr145-Oγ and the ribose 3′-OH (Figure 5B). The ATP α phosphorus shifts by 1.8 Å. The Lys170-Nζ nucleophile is 6.3 Å from the α phosphorus in an acute orientation to the pyrophosphate leaving group (Nζ–Pα–O3α angle = 66°) that is incompatible with catalysis. The contacts of Lys326 with the α and γ phosphates and of Arg4, Lys121, and Arg149 with the γ phosphate are essentially unchanged versus the Michaelis complex. Another remarkable feature of the E227A active site is that it lacks an equivalent of the non-catalytic metal seen in the Michaelis complex. Instead, E227A•ATP has a single manganese ion analogous to the

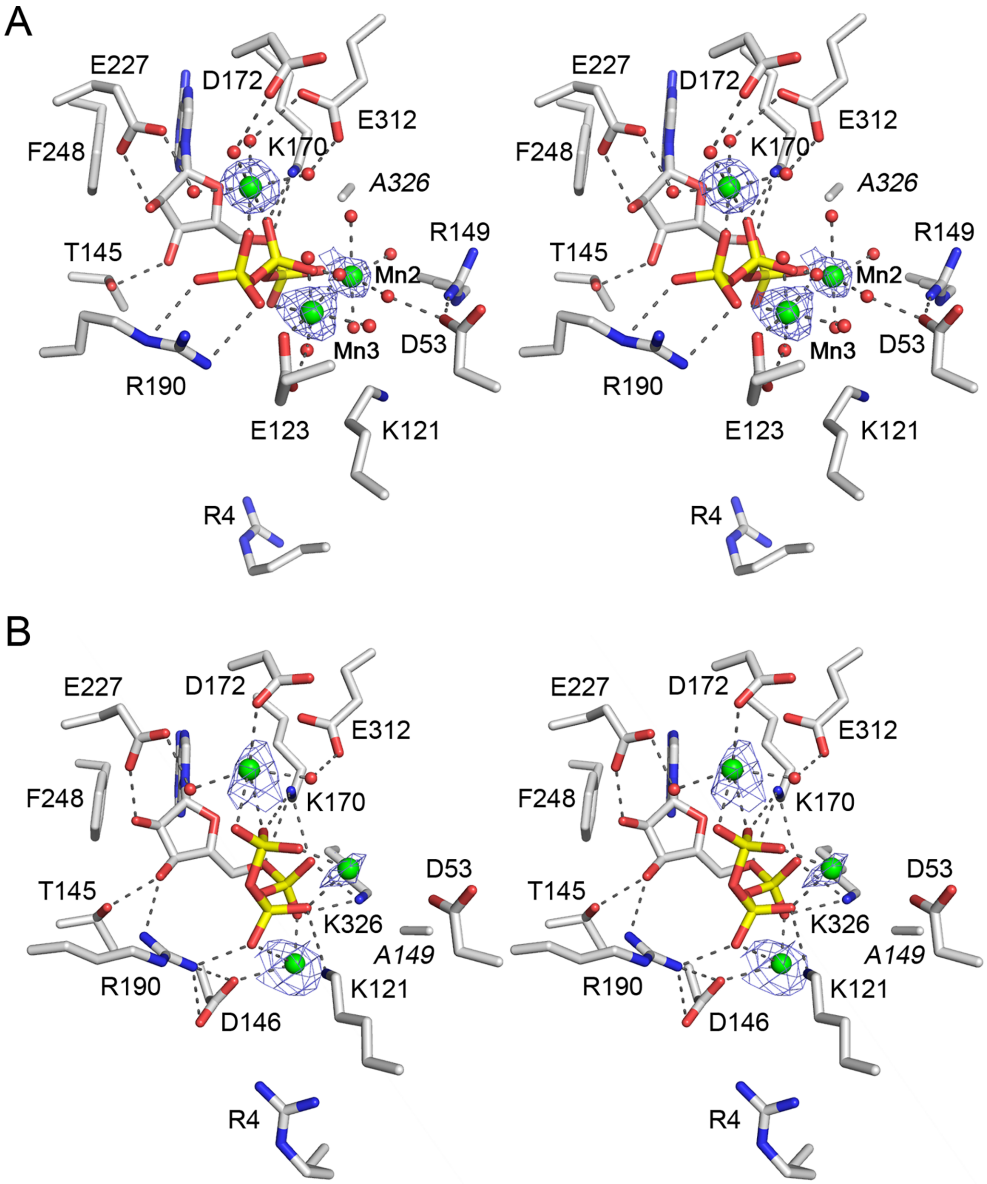

Figure 6. Off-pathway K326A•ATP•$(Mn^{2+})_3$ and R149A•ATP•$(Mn^{2+})_3$ active site structures. Stereo views of the K326A•ATP•$(Mn^{2+})_3$ (panel **A**) and the R149A•ATP•$(Mn^{2+})_3$ (panel **B**) active sites. Amino acids and ATP are rendered as stick models. The Ala mutant side chains *A326* (panel A) and *A149* (panel B) are labeled in italics. Manganese ions are depicted as green spheres; waters as red spheres. Atomic contacts are denoted by dashed lines. Anomalous difference maps around the manganese atoms are depicted in blue mesh, contoured at 2 σ.

'third' metal Mn3 observed in the K170A•ATP structure (Figure 5B). In the case of E227A, this octahedral manganese complex is filled by α, β, and γ phosphate oxygens, Asp146-Oδ, and two waters (Figure 5B). Asp146 makes a bidentate salt bridge to Arg190, tethering Arg190 in position to engage the ATP β phosphate (Figure 5B).

Off-pathway K326A•ATP•$(Mn^{2+})_3$ active site structure

The structure of the K326A•ATP complex at 1.55 Å resolution (Figure 6A) reveals how the loss of the motif V lysine contacts to the ATP α and γ phosphate oxygens leads to a re-orientation of the triphosphate moiety, with displacements of the α, β and γ phosphorus atoms by 1.7 Å, 2.0 Å, and 5.7 Å, respectively, from their positions in the Michaelis complex. Although the Lys170 nucleophile has not shifted, it now makes bifurcated hydrogens bonds from Nζ to adenosine O5′ and a β phosphate oxygen. Lys170-Nζ is 4.2 Å from the α phosphorus in an orthogonal orientation to the pyrophosphate leaving group (Nζ–Pα–O3α angle = 83°) that is unsuitable for step 1 chemistry. Whereas the catalytic manganese in the K326A active site is positioned correctly and makes the proper set of water-mediated contacts to Asp172, Glu227, and Glu312, its interactions with the ATP phosphates are perverted, such that two of the sites in the octahedral metal complex are now occupied by β and γ

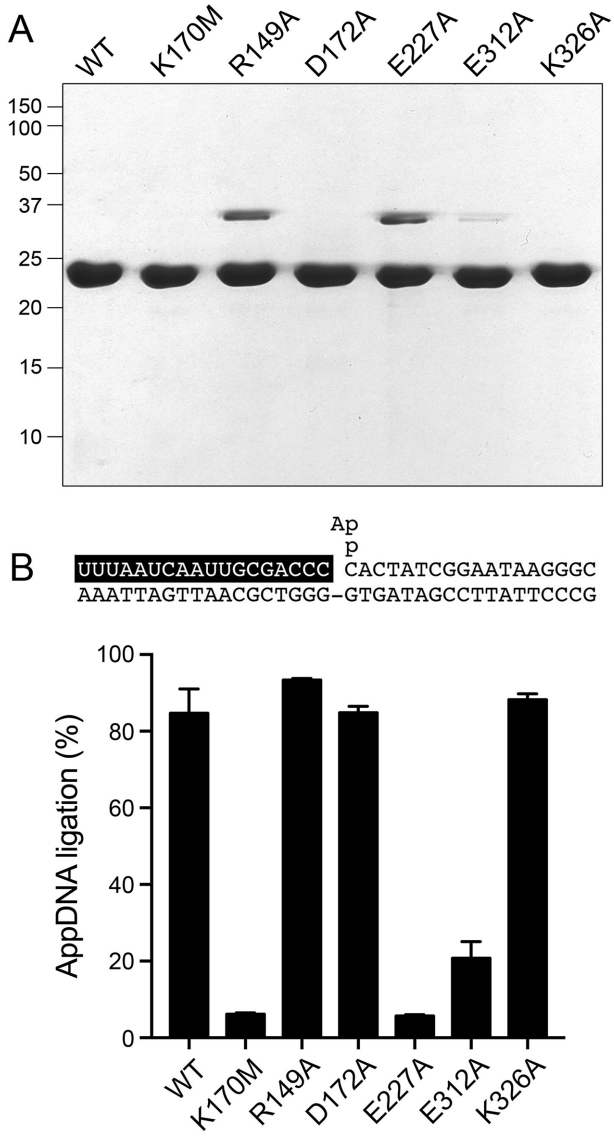

Figure 7. Mutational effects on sealing by NgrRnl-ΔN at a pre-adenylylated nick. (**A**) Recombinant NgrRnl-ΔN proteins. Aliquots (6 μg) of WT NgrRnl-ΔN and the indicated mutants were analyzed by SDS-PAGE. The Coomassie Blue-stained gel is shown. The positions and sizes (kDa) of marker polypeptides are indicated on the left. (**B**) Reaction mixtures (10 μl) containing 50 mM Tris-acetate (pH 6.0), 5 mM DTT, 5 mM $MnCl_2$, 1 pmol (0.1 μM) ^{32}P-labeled pre-adenylylated nicked duplex substrate (shown at the *top*, with the RNA strand lettered in white on a black background), and 1 pmol (0.1 μM) of WT NgrRnl-ΔN or the indicated mutant were incubated for 30 min at 37°C. The products were resolved by urea-PAGE. The extents of AppDNA ligation are plotted in bar graph format. Each datum is the average of three independent experiments ±SEM.

phosphate oxygens (in lieu of the α phosphate oxygen and a water seen at the equivalent loci in the Michaelis complex). As a result of the large movement of the γ phosphate, there are no longer any ATP contacts to Arg4, Lys121, and Arg149 (Figure 6A). Instead, Arg190 now makes a bidentate salt bridge to the γ phosphate. Most notable is the presence of two additional manganese ions in the K326A active site (labeled Mn2 and Mn3 in Figure 6A) interacting with ATP in a manner distinct from any of the preceding structures. Mn2 is coordinated octahedrally to the ATP α and β phosphate oxygens and to four waters, one of which is engaged by Asp53. Mn3 is coordinated octahedrally to a γ phosphate oxygen, the Glu123-Oε1, and four waters, one of which is in turn coordinated by Glu123-Oε2.

Off-pathway R149A•ATP•$(Mn^{2+})_3$ active site structure

As shown in Figure 6B, loss of the Arg149 contact to the ATP γ phosphate elicits a dramatic rearrangement of the triphosphate moiety, whereby the γ phosphorus atom is shifted by 5.1 Å from its positions in the Michaelis complex, while the position of the β phosphorus stays the same. The Lys170 nucleophile has not shifted, but it now makes trifurcated hydrogens bonds from Nζ to adenosine O5′, a β phosphate oxygen, and a γ phosphate oxygen. Lys170-Nζ is 3.9 Å from the α phosphorus but is situated orthogonal to the pyrophosphate leaving group (Nζ–Pα–O3α angle = 110°). With the shift in ATP conformation, Lys121 engages the β phosphate (instead of γ phosphate) and the Arg4 contact to ATP is lost. The Arg190 side chains swivels by 5.9 Å at the Cζ atom, compared to its position in the Michaelis complex, such that Arg190 now donates a hydrogen bond from NH1 to the ATP ribose 3′-OH and NH2 makes trifurcated electrostatic contacts to the β phosphate and Asp146. There are three manganese ions in the R149A•ATP complex (Figure 6B). The counterpart of the catalytic metal is engaged by Asp172, Glu227 and Glu312, but it makes contact to two of the γ phosphate oxygens instead of the α phosphate. A second metal bridges the α and β phosphates and is coordinated by Asp146. A third metal bridges the β and γ phosphates. [The Mn2 and Mn3 ligand complexes in the refined model are incomplete, insofar we did not visualize metal-bound waters.]

Effects of NgrRnl mutations on sealing at a pre-adenylylated nick

The third step of the NgrRnl ligation reaction pathway (phosphodiester formation) can be studied in isolation by assaying the sealing of a pre-adenylylated nicked duplex composed of an unlabeled 18-mer RNA 3′-OH strand and a 5′ ^{32}P-labeled 18-mer AppDNA strand annealed to a complementary 36-mer DNA template (Figure 7B). Indeed, we showed previously that the NgrRnl-ΔN protein is ∼5-fold better than the full-length NgrRnl apoenzyme in joining the RNA_{OH} and AppDNA strands (18). In order to gauge the effects of ligase-defective active site mutations on the step of phosphodiester formation, we produced and purified recombinant NgrRnl-ΔN mutants K170M, R149A, E227A, E312A, and K326A alongside the ligase-active 'WT' NgrRnl-ΔN and the D172A variant (Figure 7A). The proteins were reacted with the pre-adenylylated nicked duplex in the presence of manganese without ATP. WT NgrRnl-ΔN and the D172A protein sealed 85% of the input substrate. The instructive finding was that the K326A change, which effaced nick sealing activity in the context of full-length NgrRnl and perverted the active site for ligase-adenylylation, was benign with respect to phosphodiester synthesis. Similarly, the R149A mutation that suppressed nick sealing and warped the active site of the ATP complex

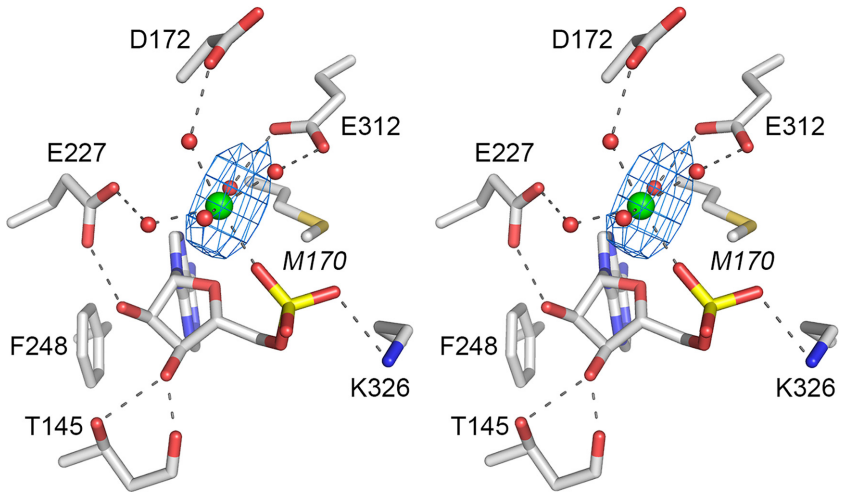

Figure 8. K170M•AMP•Mn^{2+} product complex. Stereo view of the active site. Amino acids and AMP are rendered as stick models. A manganese ion is depicted as a green sphere; waters as red spheres. Atomic contacts are denoted by dashed lines. Anomalous difference maps around the manganese atom is depicted in blue mesh contoured at 2 σ.

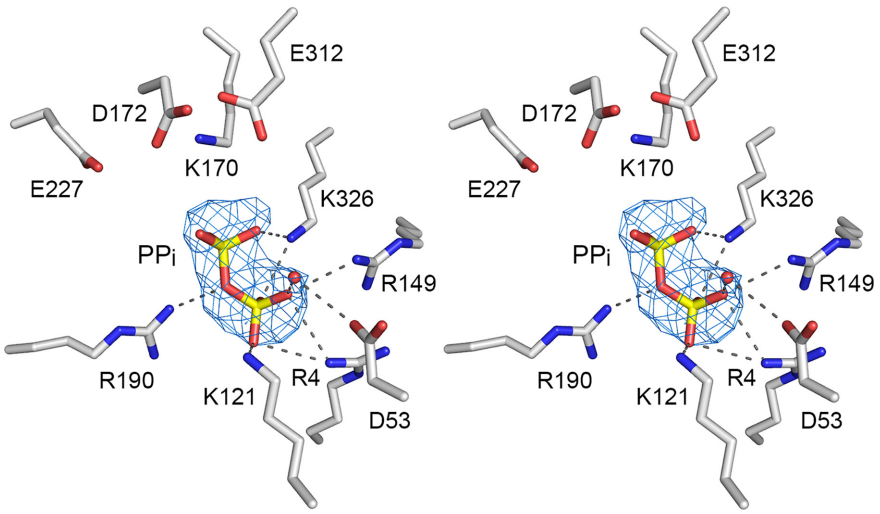

Figure 9. WT NgrRnl in complex with pyrophosphate. Stereo view of the active site. Amino acids and PP_i are rendered as stick models. A water in the position corresponding to the non-catalytic metal of the Michaelis complex is depicted as a red sphere. Atomic contacts are denoted by dashed lines. The $2F_o–F_c$ omit map around the PP_i ligand is shown in blue mesh contoured at 3 σ.

also did not impede step 3 of the ligase pathway. It is perhaps sensible that Lys326 and Arg149, both of which engage the ATP γ phosphate in the step 1 Michaelis complex, night not be critical for step 3 catalysis insofar as there is no equivalent of a γ phosphate in the 5′ adenylylated nick strand. By contrast, we find that the K170M change elicited a 14-fold reduction in the extent of AppDNA sealing *vis-à-vis* WT NgrRnl-ΔN, implying that Lys170 interaction with the AMP phosphate moiety of the AppN– nick terminus (i.e. the step 3 leaving group) abets phosphodiester synthesis. Alanine mutation of Glu227 reduced phosphodiester synthesis by 15-fold, suggesting that Glu227 contacts to the AMP ribose and/or a catalytic metal ion are important during step 3. Changing the metal-binding Glu312 to alanine reduced phosphodiester synthesis by 4-fold.

Structures of NgrRnl in binary complexes with AMP and PP_i reaction products

AMP and pyrophosphate are ligase reaction end products generated during step 3 and step 1, respectively. To attain a structure of an AMP product complex, we co-crystallized NgrRnl-K170M with AMP and manganese. The positions and enzymic contacts to AMP and the adjacent catalytic manganese ion in the AMP product complex (Figure 8) were virtually identical to those of the AMP moiety of ATP in the Michaelis complex. When we attempted to capture a complex step 1 product complex by co-crystallization of WT NgrRnl (which crystallizes *per se* as the covalent ligase-AMP intermediate in complex with a manganese ion) with 1 mM PP_i, we found that the active site contained PP_i but no nucleotide or metal (Figure 9). We speculate that addition

of PP_i to the ligase–AMP intermediate triggered regeneration of ATP via reversal of step 1, followed by dissociation of ATP from the active site and its replacement by the free PP_i present in excess. The phosphorus atoms of the PP_i are shifted by 2.3 Å and 1.5 Å compared to the β and γ phosphorus atoms of ATP in the Michaelis complex. A water coordinated to the outer phosphate of PP_i appears to be a mimetic of the non-catalytic metal ion of the Michaelis complex. Arg4, Lys121, and Arg149 engage the outer phosphate akin to their engagement of the ATP γ phosphate. Lys326 makes a bifurcated contact to both PP_i phosphates. Arg190 donates a hydrogen bond to the PP_i bridging oxygen.

DISCUSSION

The results of our alanine scan of the NgrRnl active site affirm the essentiality of several conserved amino acids in the signature NTase motifs that define the covalent lysine–nucleotidyltransferase enzyme superfamily (2). A unifying mechanism for lysine nucleotidylation by these enzymes invokes the following: (i) stabilization of the transition state on the α phosphate of the nucleotide substrate by a pentahydrated catalytic metal complex engaged via waters to amino acid side chains in motifs I, III and IV; (ii) transition state stabilization by the motif V lysine; and (iii) orientation of the leaving group apical to the motif I lysine nucleophile which, in the case of the ATP-dependent ligases, entails enzymic contacts to the γ phosphate and a non-catalytic metal that bridges the β and γ phosphates (10,15–16). Different RNA ligase families exploit distinctive structural elements in their interactions with the γ phosphate and non-catalytic metal complex, typically involving their clade-specific domain modules (10,15–16). In the case of NgrRnl, our alanine scan indicates that whereas Arg149 is important *per se* for ligase activity, the contacts of the N-terminal OB-domain residues Arg4, Lys121 and Asp53 are functionally redundant.

Previous mutational studies of exemplary RNA and DNA ligases suggested that different active site functional groups are required for the nucleotidyl transfer and phosphodiester bond formation steps of the ligation reaction pathway (23,24,26,32,39). One manifestation of this division of labor is the finding that a particular amino acid substitution inactivates 3′-OH/5′-PO_4 ligation but does not affect phosphodiester synthesis on a 5′ pre-adenylylated nucleic acid substrate, signifying that the mutated residue is necessary for step1 or step 2 but not for step 3. We see here that alanine mutation of the motif V Lys326 residue in NgrRnl eliminated 3′-OH/5′-PO_4 nick sealing and reaction of NgrRnl-K326A with ATP, yet preserved sealing at a pre-adenylylated nick. Similar findings have been reported for the analogous motif V Lys-to-Ala mutants of T4 RNA ligase 1 (26). The corresponding motif V Lys-to-Ala mutant of *D. radiodurans* RNA ligase (DraRnl) was defective for 3′-OH/5′-PO_4 nick sealing yet retained activity in ligase adenylylation (step 1) and sealing at a pre-adenylylated nick (step 3), suggesting that this lysine in DraRnl is critical for step 2 adenylate transfer to the nick 5′-PO_4 (32).

The most impactful aspect of the present study emerges from the structural analysis of the adenylylation-defective NgrRnl-Ala mutants and their complexes with ATP and manganese. The naïve expectation that an alanine change would subtract the relevant side-chain contacts without otherwise perturbing the active site interactions with substrate and cofactors was shattered in every case. Rather, we found that alanine mutations K170A, E227A, K326A, and R149A (none of which impacted overall enzyme structure) elicited dire secondary changes in the ligase active site compared to the Michaelis complex, evinced as dislocations of the ATP phosphates, altered contacts to ATP and changes in the numbers and locations of the manganese ions. These perversions forced the NgrRnl-Ala active sites into various off-pathway states, incompatible with lysine adenylylation, by virtue of the fact that: (i) the leaving group became orientated orthogonal to the lysine nucleophile; and/or (ii) key interactions of enzyme and metal with the α phosphate that stabilize the transition state were severed. We saw that each alanine mutation evoked a distinctive off-pathway aberration of the NgrRnl•ATP complex. Our results illuminate a remarkable plasticity of the ligase active site in its interactions with ATP and metals. More broadly, they underscore a valuable caveat when interpreting mutational data in the course of enzyme structure-function studies.

DATA AVAILABILITY

Structural coordinates have been deposited in Protein Data Bank under accession codes: 6VT0, 6VT1, 6VTG, 6VT3, 6VT4, 6VT5, 6VT6, 6VT8, 6VT9, 6VTB, 6VTD, 6VTE and 6VTF.

SUPPLEMENTARY DATA

Supplementary Data are available at NAR Online.

ACKNOWLEDGEMENTS

We thank Linamarie Miller for assistance with cloning, expression and purification of several NgrRnl mutants. X-ray diffraction data were collected at synchrotron facilities supported by grants and contracts from the National Institutes of Health and the Department of Energy.

FUNDING

National Institutes of Health (NIH) [R35-GM126945 to S.S.]; National Cancer Institute [P30-CA008748]. Funding for open access charge: NIH [R35-GM126945].
Conflict of interest statement. None declared.

REFERENCES

1. Shuman,S. (2009) DNA ligases: progress and prospects. *J. Biol. Chem.*, **284**, 17365–17369.
2. Shuman,S. and Lima,C.D. (2004) The polynucleotide ligase and RNA capping enzyme superfamily of covalent nucleotidyltransferases. *Curr. Opin. Struct. Biol.*, **14**, 757–764.
3. Subramanya,H.S., Doherty,A.J., Ashford,S.R. and Wigley,D.B. (1996) Crystal structure of an ATP-dependent DNA ligase from bacteriophage T7. *Cell*, **85**, 607–615.
4. Odell,M., Sriskanda,V., Shuman,S. and Nikolov,D. (2000) Crystal structure of eukaryotic DNA ligase–adenylate illuminates the mechanism of nick sensing and strand joining. *Mol. Cell*, **6**, 1183–1193.

5. Pascal,J.M., O'Brien,P.J., Tomkinson,A.E. and Ellenberger,T. (2004) Human DNA ligase I completely encircles and partially unwinds nicked DNA. *Nature*, **432**, 473–478.
6. Kaminski,A.M., Tumbale,P.P., Schellenberg,M.J., Williams,R.S., Williams,J.G., Kunkel,T.A., Pedersen,L.C. and Bebenek,K. (2018) Structures of DNA-bound human ligase IV catalytic core reveal insights into substrate binding and catalysis. *Nat. Commun.*, **9**, 2642.
7. Shi,K., Bohl,T.E., Park,J., Zasada,A., Malik,S., Banerjee,S., Tran,V., Li,N., Yin,Z., Kurniawan,F. *et al.* (2018) T4 DNA ligase structure reveals a prototypical ATP-dependent ligase with a unique mode of sliding clamp interaction. *Nucleic Acids Res.*, **46**, 10474–10488.
8. Williamson,A. and Leiros,H.S. (2019) Structural intermediates of a DNA-ligase complex illuminate the role of the catalytic metal ion and mechanism of phosphodiester bond formation. *Nucleic Acids Res.*, **47**, 7147–7162.
9. El Omari,K., Ren,J., Bird,L.E., Bona,M.K., Klarmann,G., LeGrice,S.F. and Stammers,D.K. (2006) Molecular architecture and ligand recognition determinants for T4 RNA ligase. *J. Biol. Chem.*, **281**, 1573–1579.
10. Unciuleac,M.C., Goldgur,Y. and Shuman,S. (2017) Two-metal versus one-metal mechanisms of lysine adenylylation by ATP-dependent and NAD^+-dependent polynucleotide ligases. *Proc. Natl. Acad. Sci. U.S.A.*, **114**, 2592–2597.
11. Nandakumar,J., Shuman,S. and Lima,C.D. (2006) RNA ligase structures reveal the basis for RNA specificity and conformational changes that drive ligation forward. *Cell*, **127**, 71–84.
12. Brooks,M.A., Meslet-Cladiére,L., Graille,M., Kuhn,J., Blondeau,K., Myllykallio,H. and van Tilbeurgh,H. (2008) The structure of an archaeal homodimeric ligase which has RNA circularization activity. *Protein Sci.*, **17**, 1336–1345.
13. Smith,P., Wang,L.K., Nair,P.A. and Shuman,S. (2012) The adenylyltransferase domain of bacterial Pnkp defines a unique RNA ligase family. *Proc. Natl. Acad. Sci. U.S.A.*, **109**, 2296–2301.
14. Wang,P., Chan,C.M., Christensen,D., Zhang,C., Selvadurai,K. and Huang,R.H. (2012) Molecular basis of bacterial protein Hen1 activating the ligase activity of bacterial protein Pnkp for RNA repair. *Proc. Natl. Acad. Sci. U.S.A.*, **109**, 13248–13253.
15. Unciuleac,M.C., Goldgur,Y. and Shuman,S. (2015) Structure and two-metal mechanism of a eukaryal nick-sealing RNA ligase. *Proc. Natl. Acad. Sci. U.S.A.*, **112**, 13868–13873.
16. Banerjee,A., Ghosh,S., Goldgur,Y. and Shuman,S. (2019) Structure and two-metal mechanism of fungal tRNA ligase. *Nucleic Acids Res.*, **47**, 1428–1439.
17. Peschek,J. and Walter,P. (2019) tRNA ligase structure reveals kinetic competition between non-conventional mRNA splicing and mRNA decay. *Elife*, **8**, e44199.
18. Unciuleac,M.C. and Shuman,S. (2015) Characterization of a novel eukaryal nick-sealing RNA ligase from *Naegleria gruberi*. *RNA*, **21**, 824–832.
19. Schmier,B.J. and Shuman,S. (2014) Effects of 3′-OH and 5′-PO_4 base mispairs and damaged base lesions on the fidelity of nick sealing by *Deinococcus radiodurans* RNA ligase. *J. Bacteriol.*, **196**, 1704–1712.
20. Schmier,B.J., Chen,X., Wolin,S. and Shuman,S. (2017) Deletion of the rnl gene encoding a nick-sealing RNA ligase sensitizes *Deinococcus radiodurans* to ionizing radiation. *Nucleic Acids Res.*, **45**, 3812–3821.
21. Unciuleac,M.C., Goldgur,Y. and Shuman,S. (2019) Structures of ATP-bound DNA ligase D in a closed domain conformation reveal a network of amino acid and metal contacts to the ATP phosphates. *J. Biol. Chem.*, **294**, 5094–5104.
22. Shuman,S. and Ru,X. (1995) Mutational analysis of vaccinia DNA ligase defines residues essential for covalent catalysis. *Virology*, **211**, 73–83.
23. Sriskanda,V. and Shuman,S. (1998) *Chlorella* virus DNA ligase: nick recognition and mutational analysis. *Nucleic Acids Res.*, **26**, 525–531.
24. Sriskanda,V. and Shuman,S. (2002) Role of nucleotidyl transferase motifs I, III and IV in the catalysis of phosphodiester bond formation by *Chlorella* virus DNA ligase. *Nucleic Acids Res.*, **30**, 903–911.
25. Sriskanda,V. and Shuman,S. (2002) Role of nucleotidyl transferase motif V in strand joining by *Chlorella* virus DNA ligase. *J. Biol. Chem.*, **277**, 9661–9667.
26. Wang,L.K., Ho,C.K., Pei,Y. and Shuman,S. (2003) Mutational analysis of bacteriophage T4 RNA ligase 1: different functional groups are required for the nucleotidyl transfer and phosphodiester bond formation steps of the ligation reaction. *J. Biol. Chem.*, **278**, 29454–29462.
27. Wang,L.K., Schwer,B. and Shuman,S. (2006) Structure-guided mutational analysis of T4 RNA ligase 1. *RNA*, **12**, 2126–2134.
28. Ho,C.K. and Shuman,S. (2002) Bacteriophage T4 RNA ligase 2 (gp24.1) exemplifies a family of RNA ligases found in all phylogenetic domains. *Proc. Natl. Acad. Sci. U.S.A.*, **99**, 12709–12714.
29. Yin,S., Ho,C.K. and Shuman,S. (2003) Structure-function analysis of T4 RNA ligase 2. *J. Biol. Chem.*, **278**, 17601–17608.
30. Nandakumar,J., Ho,C.K., Lima,C.D. and Shuman,S. (2004) RNA substrate specificity and structure-guided mutational analysis of bacteriophage T4 RNA ligase 2. *J. Biol. Chem.*, **279**, 31337–31347.
31. Wang,L.K. and Shuman,S. (2005) Structure-function analysis of yeast tRNA ligase. *RNA*, **11**, 966–975.
32. Raymond,A. and Shuman,S. (2007) *Deinococcus radiodurans* RNA ligase exemplifies a novel ligase clade with a distinctive N-terminal module that is important for 5′-PO_4 nick sealing and ligase adenylylation but dispensable for phosphodiester formation at an adenylylated nick. *Nucleic Acids Res.*, **35**, 839–849.
33. Cunningham,B.C. and Wells,J.A. (1989) High-resolution epitope mapping of hGH-receptor interactions by alanine-scanning mutagenesis. *Science*, **244**, 1081–1085.
34. Chakravarty,A.K. and Shuman,S. (2011) RNA 3′-phosphate cyclase (RtcA) catalyzes ligase-like adenylylation of DNA and RNA 5′-monophosphate ends. *J. Biol. Chem.*, **286**, 4117–4122.
35. Otwinowski,Z. and Minor,W. (1997) Processing of X-ray diffraction data collected in oscillation mode. *Meth. Enzymol.*, **276**, 307–326.
36. Adams,P.D., Afonine,P.V., Bunkóczi,G., Chen,V.B., Davis,I.W., Echols,N., Headd,J.J., Hung,L.W., Kapral,G.J., Grosse-Kunstleve,R.W. *et al.* (2010) PHENIX: a comprehensive Python-based system for macromolecular structure solution. *Acta Cryst.*, **D66**, 213–221.
37. Jones,T.A., Zou,J.Y., Cowan,S.W. and Kjeldgaard,M. (1991) Improved methods for building protein models in electron density maps and the location of errors in these models. *Acta Cryst.*, **A47**, 110–119.
38. Bennett,B.D., Kimball,E.H., Gao,M., Osterhout,R., Van Dien,S.J. and Rabinowitz,J.D. (2009) Absolute metabolite concentrations and implied enzyme active site occupancy in *Escherichia coli*. *Nat. Chem. Biol.*, **5**, 593–599.
39. Odell,M. and Shuman,S. (1999) Footprinting of *Chlorella* virus DNA ligase bound at a nick in duplex DNA. *J. Biol. Chem.*, **274**, 14032–14039.